SCOPE: Spectral cloud optical property estimation using real-time GOES-R longwave imagery Ⓕ

David P. Larson ⒾⒹ, Mengying Li ⒾⒹ, and Carlos F. M. Coimbra ⒾⒹ

COLLECTIONS

Ⓕ This paper was selected as Featured

View Online   Export Citation   CrossMark

SCOPE: Spectral cloud optical property estimation using real-time GOES-R longwave imagery Ⓕ

David P. Larson,[1,2] ⓘD Mengying Li,[1] ⓘD and Carlos F. M. Coimbra[1,a) ⓘD

AFFILIATIONS

[1]Department of Mechanical and Aerospace Engineering, Jacobs School of Engineering, Center for Energy Research Center for Excellence in Renewable Resources and Integration, University of California San Diego, La Jolla, California 92093-0411, USA
[2]Electric Power Research Institute, Palo Alto, California 94304, USA

[a)]Author to whom correspondence should be addressed: ccoimbra@ucsd.edu

ABSTRACT

The output of ground-based, solar power generation systems is strongly dependent on cloud cover, which is the main contributor to solar power variability and uncertainty. Cloud optical properties are typically over-simplified in forecasting applications due to the lack of real-time, accurate estimates. In this work, we introduce a method, the Spectral Cloud Optical Property Estimation (SCOPE), for estimating cloud optical properties directly from high-resolution (5-min, 2 km) imagery from Geostationary Operational Environmental Satellite (GOES)-R, which is the newest generation of the GOES system. The SCOPE method couples a two-stream, spectrally resolved radiative model with the longwave GOES-R sensor output to simultaneously estimate the cloud optical depth, cloud top height, and cloud thickness during both day and night at 5-min intervals. The accuracy of SCOPE is evaluated using one year (2018) of downwelling longwave (DLW) radiation measurements from the Surface Radiation Budget Network, which consists of seven sites spread across climatically diverse regions of the contiguous United States. During daytime clear-sky periods, SCOPE predicts DLW within instrument uncertainty ($10 \, \mathrm{W \, m^{-2}}$) for four of the seven locations, with the remaining locations yielding errors of the order of 11.2, 17.7, and $20.2 \, \mathrm{W \, m^{-2}}$. For daytime cloudy-sky, daytime all-sky (clear or cloudy), and nighttime all-sky periods, SCOPE achieves root mean square error values of 23.0–$34.5 \, \mathrm{W \, m^{-2}}$ for all seven locations. These results, together with the low-latency of the method ($\sim$1 s per sample), show that SCOPE provides a viable solution to real-time, accurate estimation of cloud optical properties for both day and night.

Published under license by AIP Publishing. https://doi.org/10.1063/1.5144350

I. INTRODUCTION

Clouds play a pivotal role in radiative transfer processes through the atmosphere. Therefore, clouds also strongly affect the output of ground-based, solar power generation systems. However, in latency-constrained applications, such as solar forecasting, clouds are typically oversimplified due to the lack of real-time, accurate estimates of cloud optical properties such as the cloud optical depth (COD). In particular, most solar forecasting methods, to date, rely on either binary (cloud or no cloud) or coarse representations of sky conditions such as clear, partly cloudy, and overcast.[1–8] In addition, data sources for estimated cloud optical properties (for a given location and time) tend to use quantized measures that are not consistent with physical quantities. For example, numerical weather prediction (NWP) models, e.g., the North American Mesoscale Forecast System (NAM), provide forecasts of cloud cover (%) per spatial grid point. While NWP forecasts of cloud cover have been used successfully as inputs for day-ahead

(>24 h) solar forecasting,[5] there is no generalized mapping from cloud cover to cloud optical properties. Therefore, we aim to provide a solution for real-time, accurate estimation of cloud optical properties that (1) can be applied to a large number of locations while (2) requiring minimal data dependencies.

While estimating physical properties from remote sensing data has been an active area of research for multiple decades,[9,10] the increasing availability of high-fidelity data presents new opportunities. Specifically, the launch of the newest generation of geostationary satellites has opened up the possibility of high temporal ($\leq$10-min) and spatial ($\leq$2 km) resolution estimates, available across the entire United States 24/7. To take advantage of this new dataset, we propose the Spectral Cloud Optical Property Estimation (SCOPE) method, a data-driven approach for estimating cloud optical properties by integrating the newest generation of satellite imagery with computationally efficient radiative modeling.[11]
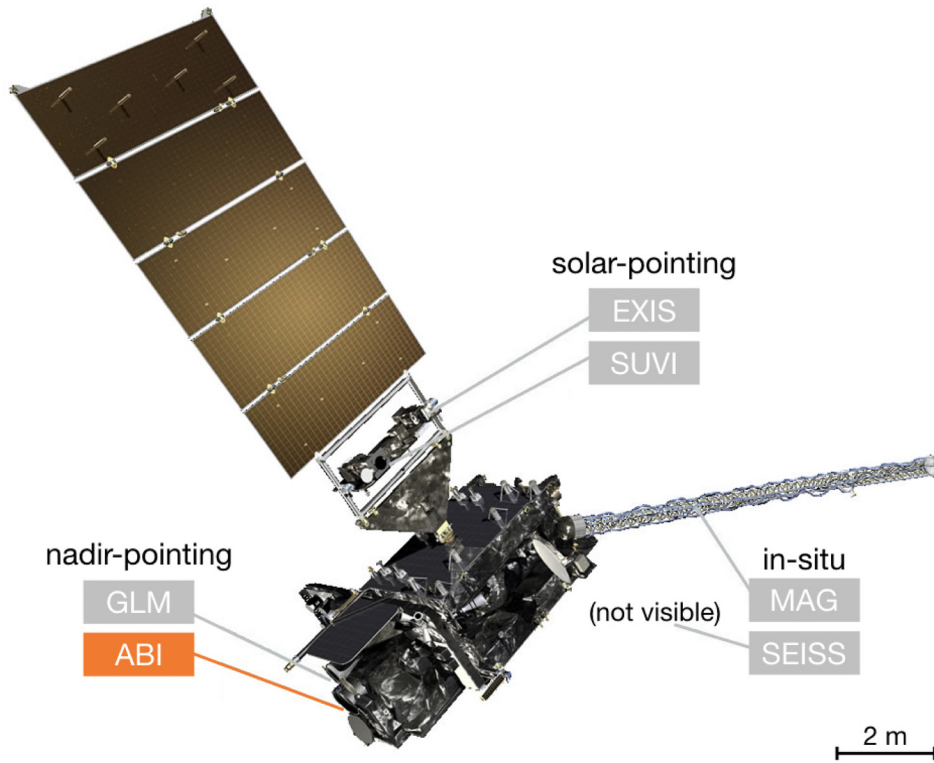
FIG. 1. Illustration of the GOES-R Series satellite design, which includes a suite of instruments: the Advanced Baseline Imager (ABI), Geostationary Lightning Mapper (GLM), Advanced Baseline Imager (ABI), Solar Ultraviolet Imager (SUVI), Extreme Ultraviolet and X-ray Irradiance Sensors (EXIS), Space Environment *In Situ* Suite (SEISS), and Magnetometer (MAG). The main satellite body has a volume of approximately 6 m × 4 m × 3 m, while the five-panel solar array is approximately 7 m × 4 m. The figure is adapted from https://www.goes-r.gov/.

At a high level, SCOPE estimates the cloud optical properties via a constrained optimization problem involving the outgoing longwave radiation (OLR) at the top of the atmosphere (TOA). Given measurements of the true OLR and a model of the OLR ($\widehat{\mathrm{OLR}}$), the cloud optical parameters are found by

$$
\begin{aligned}
\text{minimize} \quad & f(\mathrm{OLR}, \widehat{\mathrm{OLR}}(x)) \\
\text{subject to} \quad & x \in \mathcal{X},
\end{aligned} \tag{1}
$$

where $f : \mathcal{X} \to \mathbf{R}$ is the objective function. For the present study, x encodes three non-negative scalar variables: cloud optical depth [$\tau\,(-)$], cloud top height [$z_T\,(\mathrm{m})$], and cloud thickness [$\Delta z\,(\mathrm{m})$].

The rest of this paper is organized as follows: Sec. II discusses the datasets used in the development and validation of the SCOPE method. Section III details the method, as well as an analysis of the performance of the underlying radiative model. The performance of SCOPE during both day and night is presented in Sec. IV. Finally, Sec. V summarizes the key findings from this study.
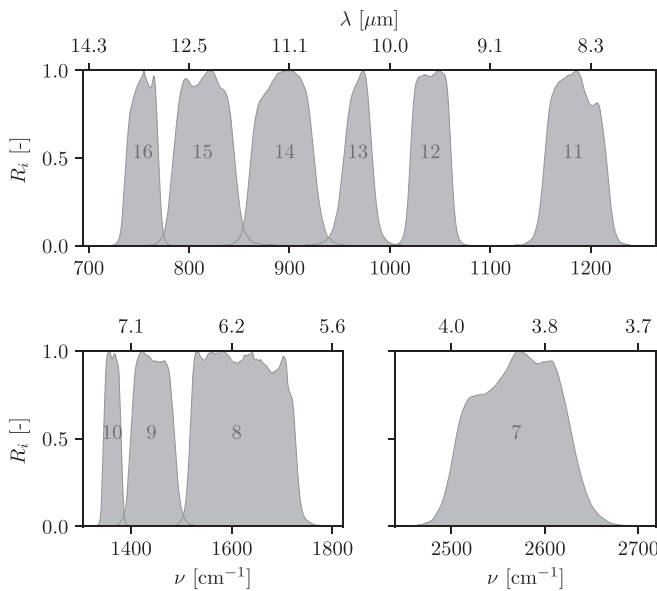
II. DATA

A. Remote sensing

We use remote sensing data from the latest generation of the Geostationary Operational Environmental Satellite (GOES) system: the GOES-R series. Operated by the National Oceanic and Atmospheric Association (NOAA), the GOES-R series consists of four identical satellites, each equipped with a suite of nadir-pointing, solar-pointing, and *in situ* instruments (see Fig. 1). Due to the focus on cloud optical properties, only data from the nadir-pointing Advanced Baseline Imager (ABI) are considered. Compared to the imagers on

the previous generation of GOES, the ABI provides data at five times the temporal resolution (full disk every 15 min and CONUS every 5 min), four times the spatial resolution (0.5–2.0 km), and three times the spectral resolution (16 spectral bands). Table I provides a summary of the ABI longwave ($\geq 4\,\mu$m) spectral bands used in this study, and Fig. 2 shows the calibrated spectral response of the channels. At the

TABLE I. Summary of the ten longwave channels from the GOES-R series ABI, in both wavelength (μm) and wavenumber (cm^{-1}) bases.[12] The center wavelengths (wavenumbers) are weighted-averages based on the integral of the spectral response function (SRF) of each channel, while the full width at half max (FWHM) wavelengths (wavenumbers) are the bandwidths corresponding to where the SRF exceeds 0.5 (50%). For a visualization of the channels and their calibrated SRF values, see Fig. 2.

Channel	Wavelength (μm)		Wavenumber (cm^{-1})	
	Center	FWHM	Center	FWHM
7	3.9	3.80–3.99	2570	2505–2630
8	6.2	5.79–6.59	1621	1517–1727
9	6.9	6.72–7.14	1444	1400–1487
10	7.3	7.24–7.43	1363	1346–1381
11	8.4	8.23–8.66	1184	1154–1216
12	9.6	9.42–9.80	1041	1020–1061
13	10.3	10.18–10.48	968	954–983
14	11.2	10.82–11.60	894	862–925
15	12.3	11.83–12.75	815	785–846
16	13.3	12.99–13.56	753	738–770

FIG. 2. The spectral response function (SRF) of each channel [R_i (–)] from calibration data of the GOES-16 ABI. Data are retrieved from http://cimss.ssec.wisc.edu/goes/calibration/. For more details on the ABI channels, see Table I.

time of this study, two GOES-R satellites are operational: GOES-16 as GOES-East (75.2° West) and GOES-17 as GOES-West (137.2° West). Due to its more direct viewing angle to the chosen testing sites and length of available operational data, all analysis presented in this work is based on GOES-16. However, similar results are expected for GOES-17 or comparable satellites, e.g., the Himawari geostationary satellites.

SCOPE uses the GOES-R ABI Level 1b Radiance product, which has a lower latency than the ABI Level 2 Cloud and Moisture Imagery (CMI) products. More specifically, SCOPE considers the band-averaged spectral radiance (mW m^{-2}sr^{-1}cm) from the ten longwave channels (7–16), which have a spatial and temporal resolution of 2.0 km and 5-min, respectively. Note that throughout this paper, we elect to refer to radiance as intensity (I), which is the nomenclature more commonly used in the radiative transfer literature. A full year of data (1/1/2018–12/31/2018) was retrieved from publicly available sources and processed to extract the intensity per channel for the pixel in the zenith direction of the target ground sites. Each ABI data file includes three UTC timestamps, corresponding to the start, center, and end of the scan. To maintain compatibility with real-time applications, the end timestamp, rounded up to the next nearest 5-min interval, is used to index the data. For example, a scan with an end timestamp of 14:27 would be indexed as 14:30. The result is one multivariate time-series per target site, consisting of eleven columns: one for the timestamp index and the remaining ten columns for the band-averaged intensity measured by the ABI longwave channels.

B. Ground telemetry

The Surface Radiation Budget Network (SURFRAD) provides long-term measurements of the surface radiation budget across the United States. There are seven active SURFRAD stations: Bondville,

Illinois (BON); Desert Rock, Nevada (DRA); Fort Peck, Montana (FPK); Goodwin Creek, Mississippi (GWN); Pennsylvania State University, Pennsylvania (PSU); Sioux Falls, South Dakota (SXF); and Table Mountain, Boulder, Colorado (TBL). Table II summarizes the stations, while Fig. 3 shows the locations of the stations from the perspective of GOES-16 and the terrain surrounding each station. Each station provides a range of irradiance and meteorological measurements at a 1-min resolution, along with quality control (QC) flags per variable. For this study, the following ground measurements are used: ambient air temperature [T_a (K)], relative humidity [ϕ (%)], global horizontal irradiance [GHI (W m^{-2})], direct normal irradiance [DNI (W m^{-2})], and downwelling longwave radiation [$F_0^\downarrow$ (W m^{-2})]. All stations measure GHI using a Spectrolab SR-75 pyranometer (0.28–3.0 μm), DNI using an Eppley Normal Incidence Pyrheliometer (NIP) (0.25–3000 μm), $F_0^\downarrow$ using an Eppley Precision Infrared Radiometer (PIR) (3.0–50.0 μm), and temperature and humidity using a sensor located 10 m off the ground. We retrieved a full year of data (1/1/2018–12/31/2018) from each of the seven stations, removed low-quality measurements (QC flags > 0), converted all variables to SI units, and then re-sampled the data to 5-min backward-averaged values to match the GOES-R CONUS scan rate. Note that only ambient air temperature and relative humidity are used as inputs to SCOPE, while GHI, DNI, and $F_0^\downarrow$ are used for validation purposes.

III. SCOPE METHOD

A. Design rationale

The goal is to estimate cloud optical properties from remote sensing data. While remote sensing data are available in the shortwave spectrum, SCOPE is designed to only consider the longwave spectrum, which provides several key benefits:

(i)   unified day and night operation: utilizing longwave data enables a unified approach for estimating cloud properties during both day and night;

(ii)   independent of view angles: longwave irradiance in the atmosphere can be approximated to be diffuse, thereby removing irradiance geometric dependencies between the position of the satellite, sun, and ground sensors;

TABLE II. Summary of the seven SURFRAD stations: three-letter station code, latitude, longitude, and Köppen climate classification. The elevation (β) and azimuth (α) look angles are from the stations to GOES-16 (GOES-East), with $\alpha = 90°$ and $\alpha = 180°$ corresponding to due East and South, respectively. For a view of the stations from GOES-16, see Fig. 3.

Station	Latitude (°)	Longitude (°)	Climate[a]	β (°)	α (°)
BON	40.1	−88.4	Dfa	41.7	160.0
DRA	36.6	−116.0	Bwk	29.9	124.6
GWN	48.3	−105.1	Bsk	27.5	142.4
FPK	34.3	−89.9	Cfa	47.2	155.0
PSU	40.7	−77.9	Dfb	42.8	175.8
SXF	43.7	−96.6	Dfa	35.2	150.4
TBL	40.1	−105.2	Bsk	34.3	138.1

[a]Köppen climate classifications: Bwk: arid, desert, cold; Bsk: arid, steppe, cold; Cfa: temperate, without dry season, hot summer; Dfa: continental, without dry season, hot summer; and Dfb: continental, without dry season, warm summer.
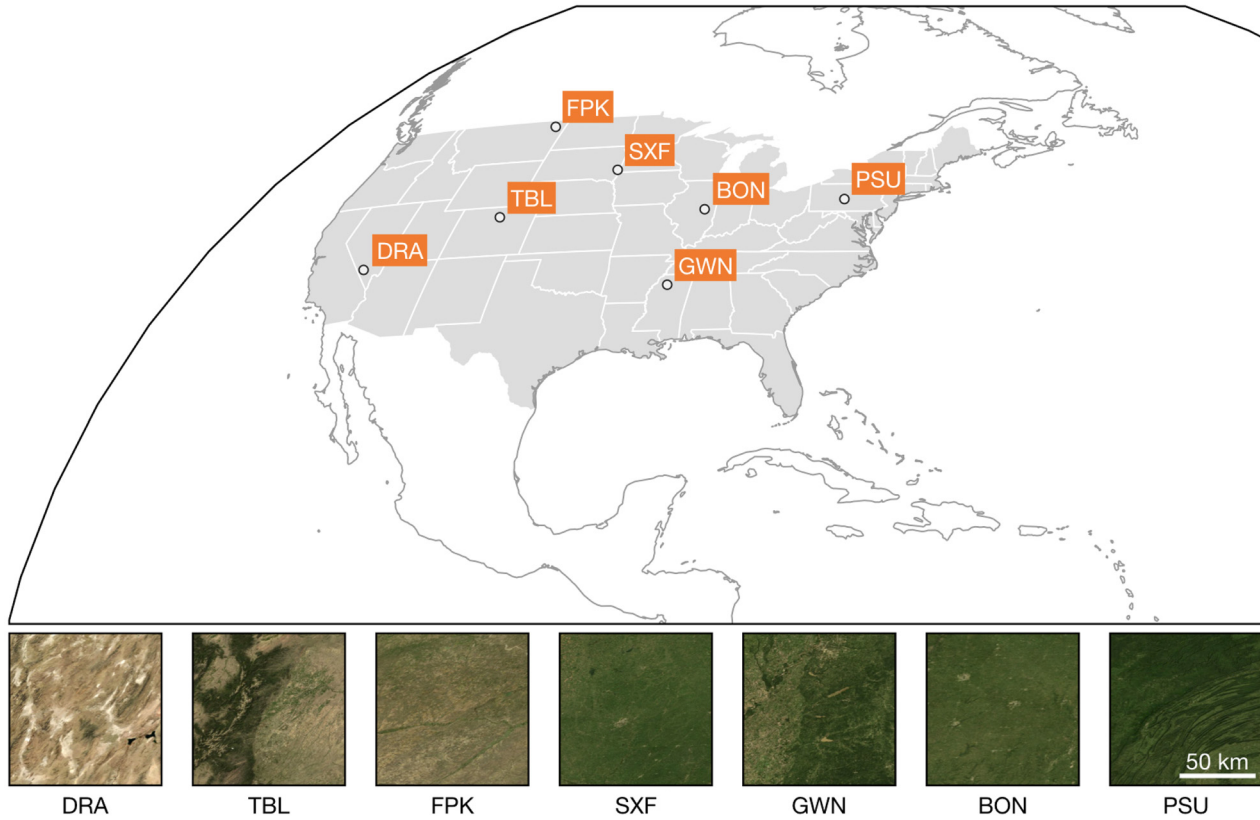
FIG. 3. Top: the view of North America from the perspective of GOES-16, cropped to match the CONUS scan area. US states are highlighted in solid gray, while the locations of the seven SURFRAD stations are denoted by circle markers. Bottom: satellite view of the $\sim$100 km $\times$ 100 km region around each SURFRAD station, ordered (left-to-right) from West to East. The satellite view highlights the climatological diversity of the stations, which cover arid desert (DRA), arid steppe (GWN, TBL), temperate (FPK), and continental (BON, PSU, SXF) climates. For more information on the SURFRAD stations, see Table II.

(iii)   two-flux approximation: because of the diffuse nature of longwave irradiance, a two-flux radiative model[13] can be used to estimate spectral longwave irradiance in the entire atmosphere at a minimal computation cost;

(iv)   surfaces approximated as black: unlike shortwaves, most surfaces (e.g., grassland, desert, and ocean) can be approximate as black in the longwave spectrum, thereby ensuring reliable performance of the method across climatically diverse regions and all seasons;

(v)   retrieve cloud temperature: the outgoing longwave irradiance also provides information about cloud top temperature (i.e., cloud altitude), while outgoing shortwave irradiance is independent of cloud temperature.

However, rather than using broadband OLR, SCOPE considers the upwelling flux from n discrete spectral bands [$F_i^\uparrow$ (W m^{-2})]

$$\text{minimize} \quad \sum_{i=1}^{n} f\left(F_i^\uparrow, \widehat{F}_i^\uparrow(x)\right)$$
$$\text{subject to} \quad x \in \mathcal{X}, \tag{2}$$

where $\widehat{F}_i^\uparrow$ is a model of $F_i^\uparrow$ and x encodes the cloud optical properties.

There are two primary reasons for the choice of using $\widehat{F}_i^\uparrow$. First, the GOES-R ABI and related imagers measure over discrete channels.

While broadband OLR can be approximated from discrete spectral measurements,[14] the additional latency required is prohibitive for our use case. Second, the spectral response of clouds varies throughout the longwave spectrum, providing additional information that can be leveraged to estimate cloud properties.

B. Overview of the radiative model

SCOPE estimates cloud optical properties by comparing the satellite measurement with radiative modeling results. To balance both accuracy and computational performance, SCOPE uses the two-stream, line-by-line longwave radiative model from the study by Li *et al.* (2018).[11] The atmosphere from the surface to 120 km is modeled as multiple plane-parallel layers, with the layer boundaries defined by a pressure coordinate system. The vertical profiles of atmospheric gases are adapted from standard Air Force Geophysical Laboratory (AFGL) midlatitude profiles with corrections for current surface conditions, including water vapor, which is adjusted based on surface measurements of T_a and ϕ.[11,15] The line-by-line absorption coefficients of atmospheric gases are retrieved from the HITRAN database and MT_CKD continuum model.[16,17] The optical properties of aerosols are modeled by Mie theory with the aerosol vertical profile adapted from CALIPSO measurements.[11] The optical properties of

plane-parallel clouds are modeled again by Mie theory with predefined droplet distribution (effective radius of 10 μm and variance of 0.1).[18] Anisotropic scattering of aerosols and clouds is scaled as isotropic by $\delta-$M approximation,[19] which is found to be sufficiently accurate for the considered longwave spectrum.[20] With each layer being diffuse and isotropic after the scaling, a two-flux approach is used to recursively compute spectral upwelling and downwelling fluxes at all layer boundaries.[11]

The radiosity (J) and irradiation (G) of each layer are then calculated by solving the following linear system for every wavenumber $\nu \in \{\nu_1, \nu_2, \ldots, \nu_n\}$:

$$\begin{pmatrix} G \\ J \end{pmatrix} = \begin{bmatrix} 0 & \mathcal{F} \\ \widehat{\rho} & 0 \end{bmatrix} \begin{pmatrix} G \\ J \end{pmatrix} + \begin{pmatrix} 0 \\ (1-\widehat{\rho})B \end{pmatrix}, \qquad (3)$$

where $G \in \mathbf{R}^{N+2}$ is the irradiation per layer

$$G := \begin{pmatrix} G_0 \\ G_1 \\ \vdots \\ G_{N+1} \end{pmatrix}, \qquad (4)$$

the elements of $J \in \mathbf{R}^{N+2}$ contain the radiosity of each layer,

$$J := \begin{pmatrix} J_0 \\ J_1 \\ \vdots \\ J_{N+1} \end{pmatrix}, \qquad (5)$$

and the matrix $\widehat{\rho} \in \mathbf{R}^{(N+2)\times(N+2)}$ contains the values for single scattering albedo of each layer,

$$\widehat{\rho} := \begin{bmatrix} \widehat{\rho}_0 & 0 & \ldots & 0 \\ 0 & \widehat{\rho}_1 & \ldots & 0 \\ \vdots & \vdots & \ddots & \vdots \\ 0 & 0 & \ldots & \widehat{\rho}_{N+1} \end{bmatrix}. \qquad (6)$$

The coefficients in $\mathcal{F} \in \mathbf{R}^{(N+2)\times(N+2)}$ are the transfer factors between layers, which are calculated using the optical depth and scattering of all layers,[11]

$$\mathcal{F} := \begin{bmatrix} \mathcal{F}_{0,0} & \mathcal{F}_{0,1} & \ldots & \mathcal{F}_{0,N+1} \\ \mathcal{F}_{1,0} & \mathcal{F}_{1,1} & \ldots & \mathcal{F}_{1,N+1} \\ \vdots & \vdots & \ddots & \vdots \\ \mathcal{F}_{N+1,0} & \mathcal{F}_{N+1,1} & \ldots & \mathcal{F}_{N+1,N+1,} \end{bmatrix}, \qquad (7)$$

and the coefficients in $B \in \mathbf{R}^{N+2}$ correspond to the blackbody emissive power of each atmospheric layer,

$$B := \begin{pmatrix} \pi\bar{I}_{b,0} \\ \pi\bar{I}_{b,1} \\ \vdots \\ \pi\bar{I}_{b,N+1} \end{pmatrix}. \qquad (8)$$

The upwelling and downwelling flux at the layer boundaries is then computed from the radiosity and irradiation. The computational performance is improved when using the plating algorithm from the study by Edwards (1986) to solve the linear equations recursively, rather than via direct matrix inversion, as discussed in the study by Li et al. (2018).[11,21] The grid convergence test in Appendix B shows that a 32-layer atmosphere with a spectral resolution of 0.1 cm^{-1} meets the accuracy requirements of SCOPE. For further details on the radiative model, see the study by Li et al. (2018) and subsequent papers.[11,15,22]

C. Approximate local atmospheric conditions

To approximate the time-varying and location dependent vertical temperature profile of the local atmosphere, SCOPE uses a linear correction to the standard AFGL midlatitude summer temperature profile, as illustrated in Fig. 4(a) for the daytime and Fig. 4(b) for the nighttime. The troposphere (0–14 km) temperature is linearly corrected using T_a to match local conditions. During the nighttime, a temperature inversion is assumed to occur at 1 km above the ground. The linear correction of the temperature profile is the representative of local atmospheric conditions, as validated in Fig. 7, where the modeled and satellite measured fluxes per channel show good agreement.
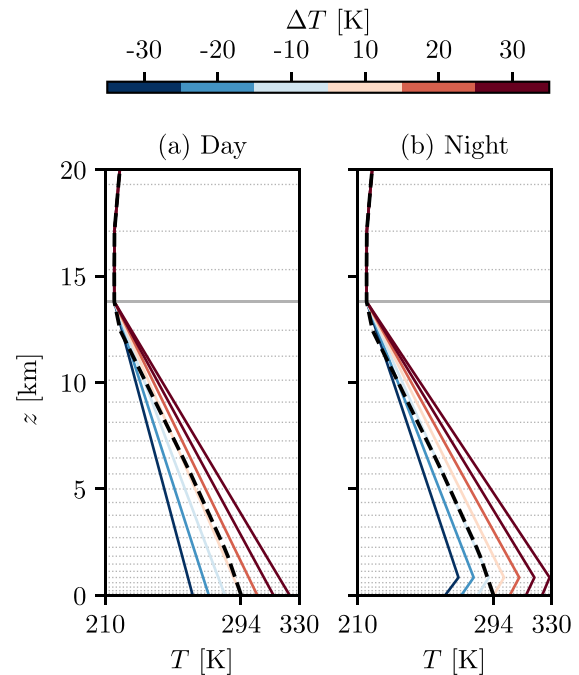
FIG. 4. Illustration of the temperature profiles [$T(z)$ (K)] used as input to the radiative model for (a) day and (b) night. The AFGL midlatitude summer profile is used as the base profile (thick black dashed line), and then the temperature in the troposphere is linearly interpolated from the tropopause to the surface temperature, with the night profiles including an inversion. The line colors denote ΔT, the difference between the original surface temperature provided by the AFGL profile (294.2 K) and the measured ambient temperature (T_a). The heights (z) of the model layers (32-layer discretization) are shown as dotted gray lines. For 2018, the seven SURFRAD stations recorded temperatures between 233 K ($-40\,^\circ$C) and 315 K (42 $^\circ$C), which correspond to ΔT values from -61 K to 21 K for the AFGL midlatitude summer profile.

D. Outgoing flux per channel

From the channel-averaged spectral intensity [I_ν (W m^{-2} sr^{-1} cm)] provided by the GOES-R ABI Level 1b Radiance product, the upwelling flux per channel i is computed as

$$F_i^\uparrow = \pi I_{\nu,i} \int R_i(\nu) d\nu, \qquad (9)$$

where R_i (−) is the SRF per channel i from the ABI calibration, as shown in Fig. 2.

Similarly, given the modeled spectral intensity ($\widehat{I}_\nu$), the modeled flux per channel ($\widehat{F}_i^\uparrow$) is computed as

$$\widehat{F}_i^\uparrow = \pi \int \widehat{I}_{\nu,i}(\nu) R_i(\nu) d\nu. \qquad (10)$$

One complication to using $F_i^\uparrow$, rather than the broadband OLR, is that $F_i^\uparrow$ varies by more than an order of magnitude across the longwave spectral range of 0–3000 cm^{-1}. To prevent channels with large $F_i^\uparrow$ magnitudes from biasing the estimates of cloud properties, SCOPE uses normalized $F_i^\uparrow$ values [F_i^* (−)],

$$F_i^* = F_i^\uparrow / E_{b,i}(T), \qquad (11)$$

where $E_{b,i}$ (W m^{-2}) is the blackbody emissive power per channel i at temperature T. Throughout this work, surface temperature T_a will be used as T. After normalization, each channel receives uniform weight in the later optimization process.

E. Estimation cloud optical properties

To identify spectral channels for cloud estimation, the spectral outgoing longwave irradiance with respect to the primary input parameters (T_a, ϕ, τ, z_T, Δz) is analyzed using the radiative model. Based on the underlying physics of radiative transfer in the atmosphere, the spectral $F_\nu^\uparrow$ is dependent on the primary model parameters in the following ways, as illustrated in Figs. 5 and 6:

(i)   decreasing T_a causes $F_\nu^\uparrow$ to decrease as colder ground emits less longwave radiation, thus less radiation transmitted through the atmosphere to the outer space;

(ii)   increasing ϕ causes $F_\nu^\uparrow$ to decrease as water vapor attenuates longwave radiation emitted by the ground;

(iii)   increasing τ increases cloud attenuation of ground longwaves to the outer space and replaces ground with colder clouds, thereby decreasing $F_\nu^\uparrow$;

(iv)   increasing z_T causes $F_\nu^\uparrow$ to decrease as higher altitude clouds are colder and therefore emit less longwave radiation;

(v)   increasing Δz causes $F_\nu^\uparrow$ to decrease as thicker clouds attenuate more radiation.

The relevant spectral ABI channels are readily identified from Fig. 6:

(i)   channels 7 (shortwave window), 11 (cloud-top phase), and 13–15 (longwave windows) respond most strongly to changes in T_a and τ;

(ii)   channels 11 and 13–15 show the largest relative responses to z_T and Δz;

(iii)   channels 8–10 respond to z_T, but are invariant to changes in τ.

Therefore, we select channels 8–10 to estimate z_T and then use channels 11 and 13–15 to estimate corresponding τ and Δz. Algorithm 1 outlines the main steps of SCOPE.
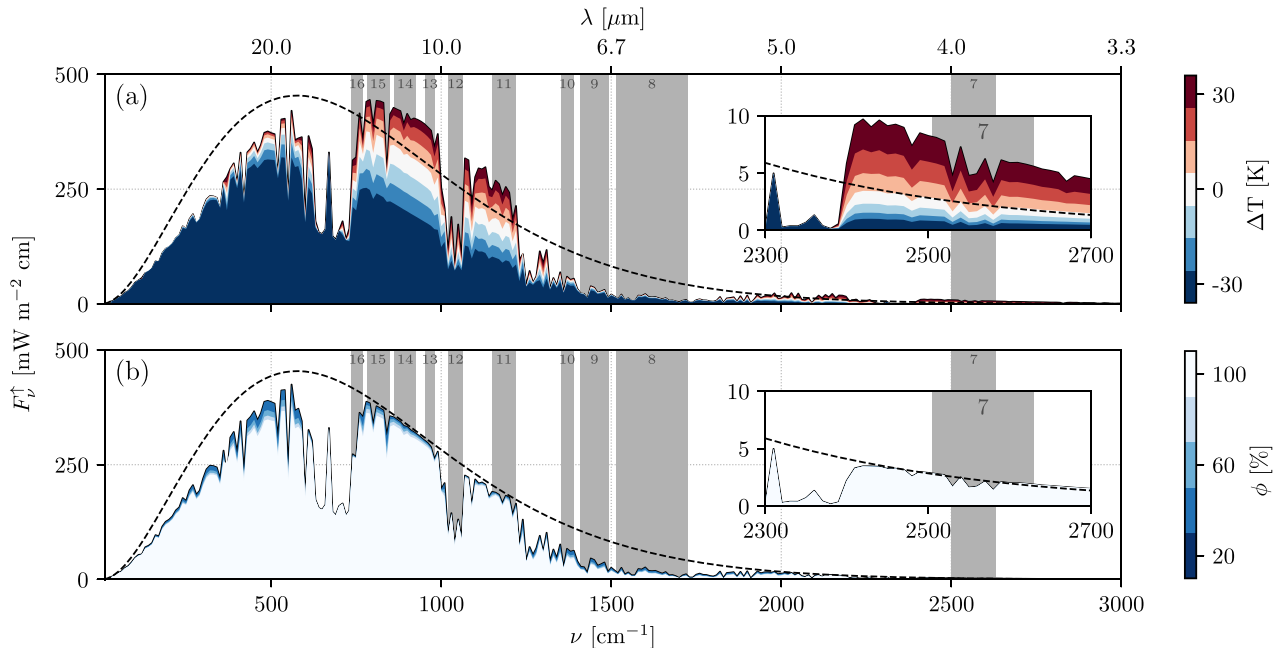
FIG. 5. The clear-sky upwelling spectral flux at TOA [$F_\nu^\uparrow$ (mW m^{-2} cm)] as a function of (a) T_a at the surface ($\tau = 0$, $\phi = 50\%$) and (b) ϕ at the surface ($\tau = 0$, $\Delta T = 0$ K). Note that the spectral flux is shown with a resolution of 10 cm^{-1} for improved readability and that (a) shows the temperature difference from the AFGL midlatitude summer profile surface temperature ($\Delta T = T - T_0$, where $T_0 = 294$ K), rather than T_a, for ease of interpretation. For all the plots, the location and bandwidth of the ten longwave ABI channels (7–16) are highlighted, with the inset plots added to better show the spectral range that contains channel 7 (2300–2700 cm^{-1}). The black dashed line in each subplot shows the blackbody spectral emissive power ($E_{b,\nu}$) at $T = 294$ K.
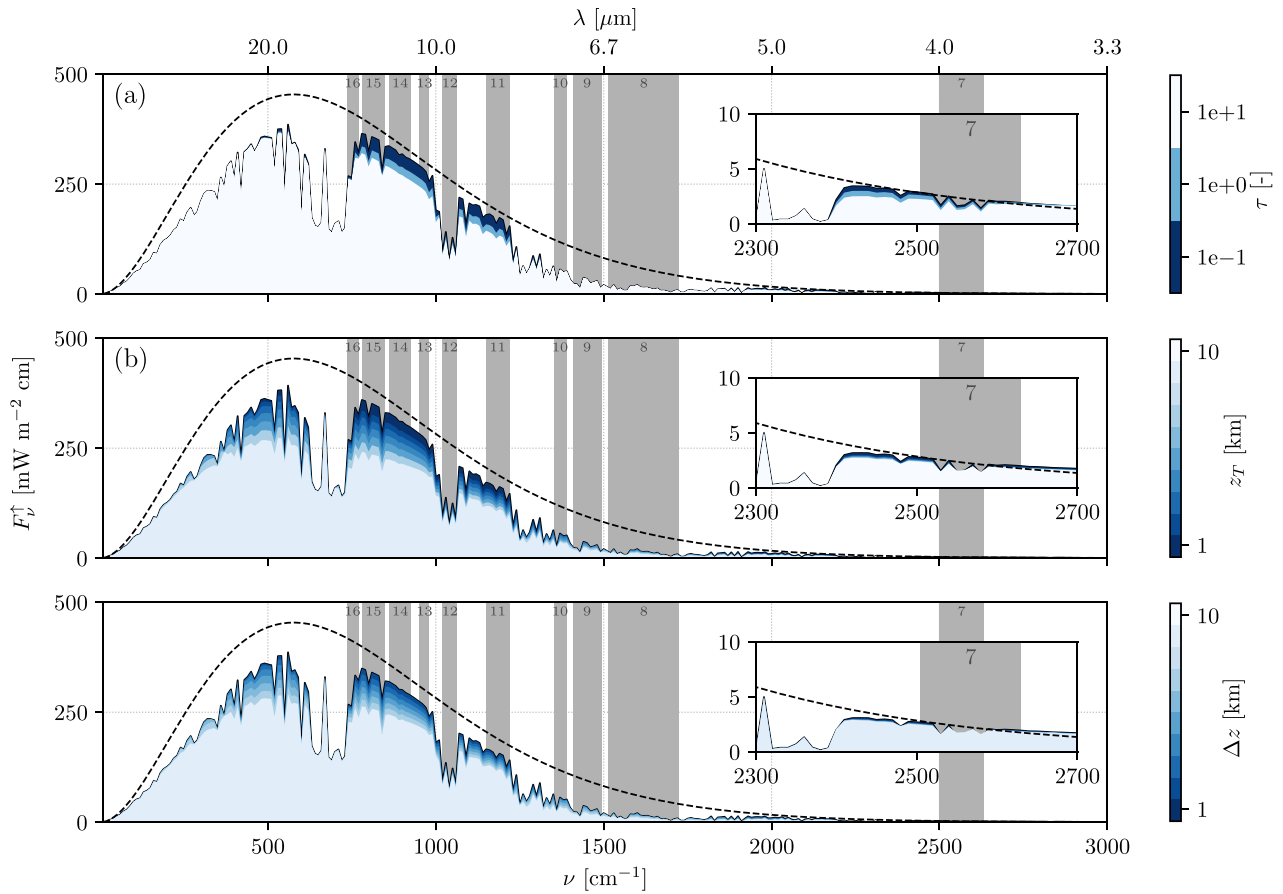
FIG. 6. The upwelling spectral flux at TOA [$F_\nu^\uparrow$ (mW m^{-2} cm)] as a function of (a) cloud optical depth τ, (b) cloud top height z_T, and (c) cloud thickness Δz, with all other parameters fixed as follows: (a) $z_T = 3.2$ km (thickness: 0.5 km; cloud average temperature: 279 K), $T_a = 294$ K, and $\phi = 50\%$; (b) $\tau = 0.1$, $T_a = 294$ K, and $\phi = 50\%$; (c) $\tau = 1.0$, $z_B = 1.84$ km, $T_a = 294$ K, and $\phi = 50\%$. All other formatting details are identical to those in Fig. 5.

Algorithm 1: Spectral Cloud Optical Property Estimation (SCOPE)

Input: T_a, ϕ, $I_{7,\nu}^\uparrow$, $I_{8,\nu}^\uparrow$, ..., $I_{16,\nu}^\uparrow$

Output: $\widehat{\tau}$, $\widehat{z}_T$, $\widehat{\Delta z}$

1 for $i \in \{7, ..., 16\}$ **do**

2    $F_i^\uparrow = \pi I_{i,\nu}^\uparrow \int R_i(\nu) d\nu$;   //upwelling flux

3    $E_{b,i} = \int E_b(\nu) d\nu$;   // blackbody flux

4    $F_i^* = F_i^\uparrow / E_{b,i}$;   // normalized flux

5 end

6 classify the current sky as clear or cloudy;

7 if $sky == cloudy$ **then**

8    $\widehat{z}_T = \arg\min\limits_{z_T} \sum\limits_{i \in \{8,9,10\}} f(F_i^*, \widehat{F}_i^*(z_T; T_a, \phi))$ // estimate z_T

9    $\widehat{\tau}, \widehat{\Delta z} = \arg\min\limits_{\tau, \Delta z} \sum\limits_{i \in \{7,11,13,14,15\}} f(F_i^*, \widehat{F}_i^*(\tau, \Delta z; T_a, \phi, \widehat{z}_T))$;   // estimate τ and $\widehat{\Delta z}$

10 else

11    $\widehat{\tau} = 0$, $\widehat{z}_T = 0$, $\Delta z = 0$;

12 end

13    $\widehat{F}_0^\downarrow = F_0^\downarrow(T_a, \phi, \widehat{\tau}, \widehat{z}_T, \widehat{\Delta z})$;   // model $F_0^\downarrow$ using estimated properties

---

SCOPE is implemented in Python 3 using standard scientific Python libraries: numpy, scipy, and pandas. In addition, to minimize computational latency and therefore meet the goal of $\ll 60$ s per time instance, the current implementation uses a pre-computed lookup table of T_a, ϕ, τ, z_T, and Δz combinations for $\widehat{F}_i^*$ and $\widehat{F}_0^\downarrow$,

- $T_a \in [234, 324]$ K,
- $\phi \in [10, 100]$ %,
- $\tau \in [0.1, 100.0]$,
- $z_T \in [1.5, 11.2]$ km,
- $\Delta z \in [0.2, 10.1]$ km,

where T_a is discretized in steps of 10 K from the AFGL midlatitude summer profile's surface temperature (294 K), τ is discretized according to 10^x with $x \in \{-1.0, -0.8, ..., 1.8, 2.0\}$, and $(z_T, \Delta z)$ are discretized according to the pressure coordinate system of the radiative model. Note that combinations of z_T and Δz are restricted to values consistent with real-world clouds. The lookup table is used in place of directly calling the radiative model iteratively, thereby reducing the overall run time of the method. Specifically, at each time t, the modeled $\widehat{F}_i^*$ are linearly interpolated to the $T_a(t)$ and $\phi(t)$ from ground measurements, and then $(\tau, z_T, \Delta z)$ are estimated from comparing
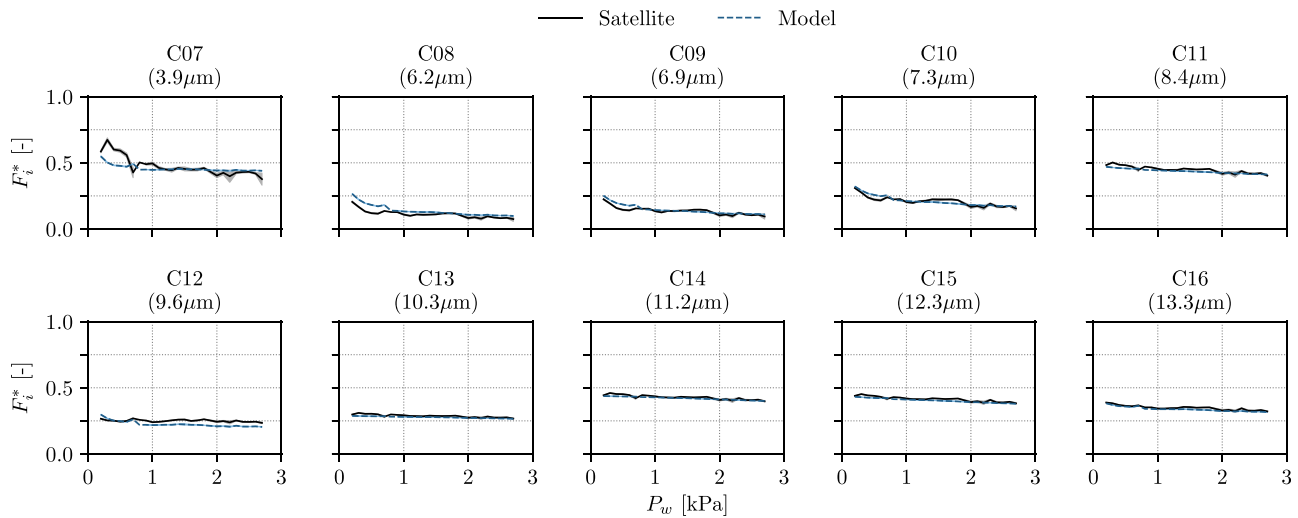
FIG. 7. Comparison of the normalized upwelling flux per channel i (F_i^*) measured by the GOES-16 ABI (Satellite) and estimated by the longwave model (Model) for the ten longwave channels (7–16) vs the water vapor partial pressure [P_w (kPa)] at the surface. The data in the plots cover one full year (1/1/2018–12/31/2018) of daytime clear-sky periods for the PSU SURFRAD station. For each time t, the upwelling flux is normalized by the blackbody radiation predicted by Planck's distribution using the measured surface temperature ($T_a(t)$). Then, the fluxes are grouped into P_w bins of width 0.1 kPa, with the mean values shown as the lines and the solid fill-in areas showing the 95% confidence interval (CI). Higher P_w values are correlated with higher concentrations of water vapor in the air.

modeled $\widehat{F}_i^*$ with satellite measurements. On a standard workstation-class computer, the total wall-clock time for the estimation method using the lookup table is ~1 s per timestamp.

IV. SCOPE RESULTS

The accuracy of the proposed SCOPE method on four types of sky conditions is evaluated: (1) daytime clear, (2) daytime cloudy, (3) daytime all-sky (clear and cloudy), and (4) nighttime all-sky. For the daytime periods ($\theta_z \leq 85°$), a clear-sky identification method, based on measured GHI, separates the data into daytime clear and daytime cloudy datasets.[23] Over one full year (1/1/2018–12/31/2018), ~15% of the daytime data from all seven sites (~350 000 samples total at a 5-min resolution) is identified as clear, with individual sites having ~5% (PSU) to ~35% (DRA) of their daytime data identified as clear.

Due to the lack of measurements of ($\tau, z_T, \Delta z$) at the SURFRAD sites, the performance of the SCOPE method is analyzed using a two-part validation. First, the accuracy of the method in reproducing $F_i^\uparrow$ across the ten longwave channels is evaluated. If the ($\tau, z_T, \Delta z$) estimates are correct, then the measured and modeled fluxes should match for all ten channels. Second, the measured downwelling longwave irradiance at the surface ($F_0^\downarrow$) is compared with the $F_0^\downarrow$ modeled by the radiative model ($\widehat{F}_0^\downarrow$) using the estimated ($\tau, z_T, \Delta z$). Since the PIR instruments at the SURFRAD sites have a spectral range of $\nu_1 = 200$ cm^{-1} to $\nu_2 = 3333$ cm^{-1}, $\widehat{F}_0^\downarrow$ is computed as

$$\widehat{F}_0^\downarrow = \pi \int_{\nu_1}^{\nu_2} \widehat{I}_\nu^\downarrow d\nu, \qquad (12)$$

where $\widehat{I}_\nu^\downarrow$ is the downwelling spectral intensity at the surface (W m^{-2} sr^{-1} cm).

A. Daytime clear periods

First, the method is validated on clear-sky periods (COD = 0) during daylight hours. Figure 7 provides a visualization of F_i^* as a function of the water vapor partial pressure (P_w). The visualization only shows the results for one station (PSU), but all seven stations exhibit similar results (see Appendix C for the corresponding figures for the other six stations). Namely, the measured and modeled F_i^* agree across the range of observed P_w values, with F_i^* decreasing as P_w increases, which corresponds to increased levels of water vapor content and therefore increased attenuation of longwave radiation. Figure 8 shows the root mean square error (RMSE) and MBE of the F_i^* for the ten long-wave channels and seven stations. Overall, the seven stations show similar levels of RMSE and MBE in each channel, with the largest error and variation in error among the stations in channel 7. Known as the short-wave window, channel 7 lies at the boundary of the shortwave-longwave spectral ranges and has a known reflected solar component during the day. As will be discussed in Sec. IV D, the lower error in channel 7 in the nighttime all-sky case indicates that the higher channel 7 error is due to the reflected solar component. However, the higher channel 7 F_i^* error during the day is not sufficient to have a noticeable effect on the accuracy of the ($\tau, z_T, \Delta z$) estimation, as measured by the $F_0^\downarrow$ error.

To further validate the method during clear-sky periods, $F_0^\downarrow$ from the radiative model is compared against measurements from a PIR instrument at each station. Figure 9 compares the RMSE and MBE of the daytime clear-sky $F_0^\downarrow$ at the stations. The RMSE for four of the seven stations (BON, FPK, GWN, and SXF) is less than or approximately the same as the uncertainty of the PIR instrument (± 5 W m^{-2}). Of the remaining three stations, one (PSU) exhibits a RMSE of nearly within instrument uncertainty (11.2 W m^{-2}), with the other two (DRA and TBL) being the furthest west of the seven stations and therefore at the most extreme look angles from GOES-16. In
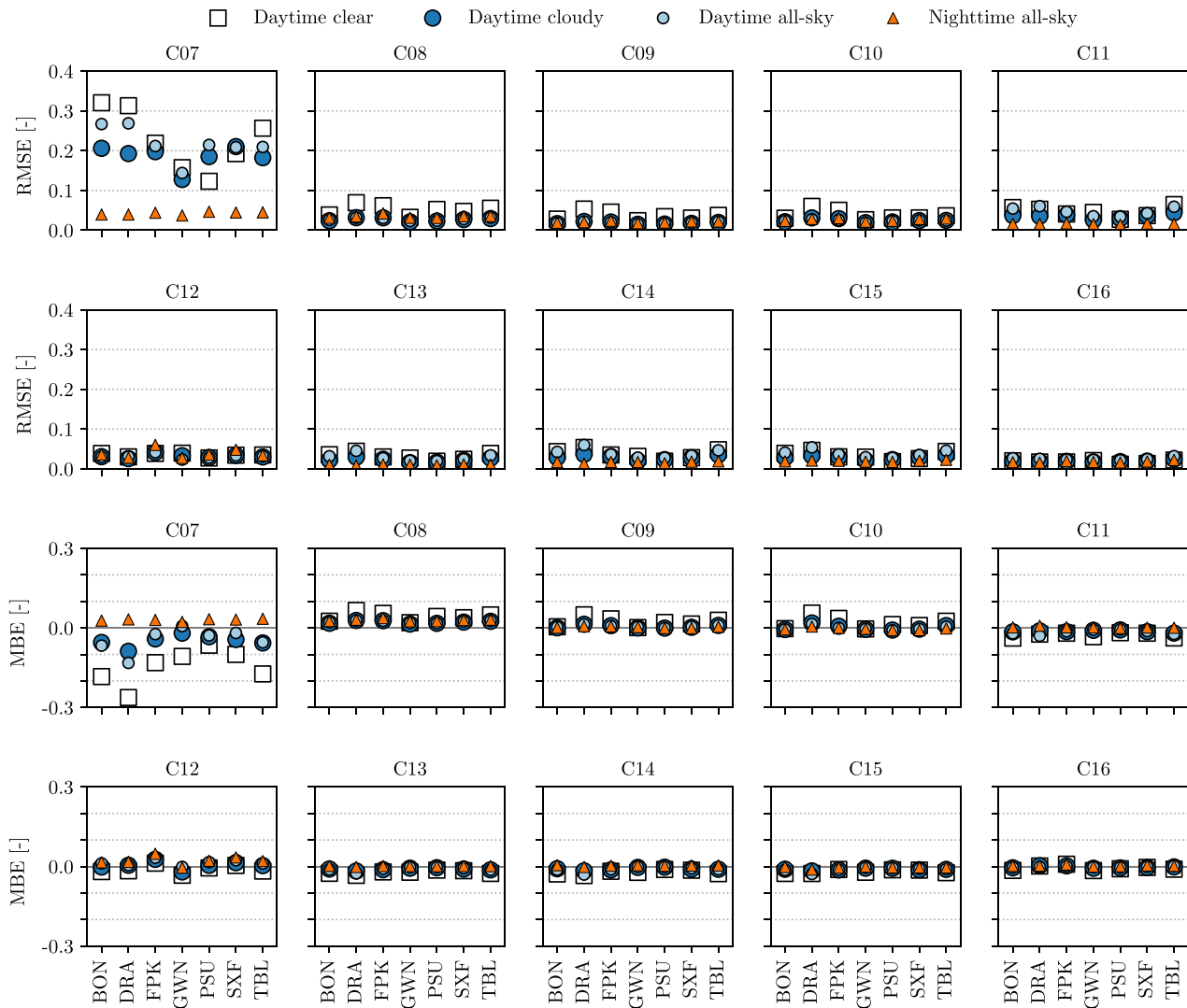
FIG. 8. The RMSE and MBE between the measured and modeled normalized upwelling flux per channel [F_i^* ($-$)] for the ten longwave channels (7–16), seven SURFRAD stations, and four evaluated cases: (1) daytime clear-sky (open square), (2) daytime cloudy-sky (large solid circle), (3) daytime all-sky (clear or cloudy) (small solid circle), and (4) nighttime all-sky (clear or cloudy) (solid triangle). The division between the daytime and the nighttime is based on the solar zenith angle, with the clear vs cloudy periods segmented using ground measurements of GHI. For the daytime clear-sky case, τ is set to zero, whereas for the other three cases, τ, z_T, and Δz are estimated at each time step from F_i^* using SCOPE. The larger RMSE and MBE magnitudes in channel 7 (shortwave window) during the daytime can be attributed to the fact that channel 7 contains a reflected solar component during the day, which is not present at night. For more information, see the GOES-R ABI documentation: https://www.goes-r.gov/.

addition, DRA and TBL have the highest elevations of seven at 1007 m and 1689 m, respectively. The extreme look angles and high elevations of DRA and TBL may be the cause of the large error, but further testing, e.g., of other sites with similar look angles and elevations, is required to provide a conclusive answer.

B. Daytime cloudy periods

The SCOPE method is then evaluated on daytime cloudy-sky periods. Here, SCOPE estimates τ, z_T, and Δz based on F_i^*, which are then validated using $F_0^\downarrow$. Figures 8 and 9 visualize the F_i^* and $F_0^\downarrow$ error, respectively, for the daytime cloudy-sky case. The RMSE and MBE of

the F_i^* under cloudy-sky conditions are comparable to those under clear-sky conditions, with the highest error in channel 7. As expected, the RMSE and MBE of the cloudy-sky $F_0^\downarrow$ are higher than those of the clear-sky as τ, z_T, and Δz are unknown *a priori*. In addition, the daytime cloudy-sky $F_0^\downarrow$ is under-predicted (MBE < 0) for all sites except TBL, indicating that SCOPE either over-estimated z_T or under-estimated Δz.

C. Daytime all-sky periods

The method is evaluated for daytime all-sky conditions, which includes both clear and cloudy conditions. First, to minimize errors
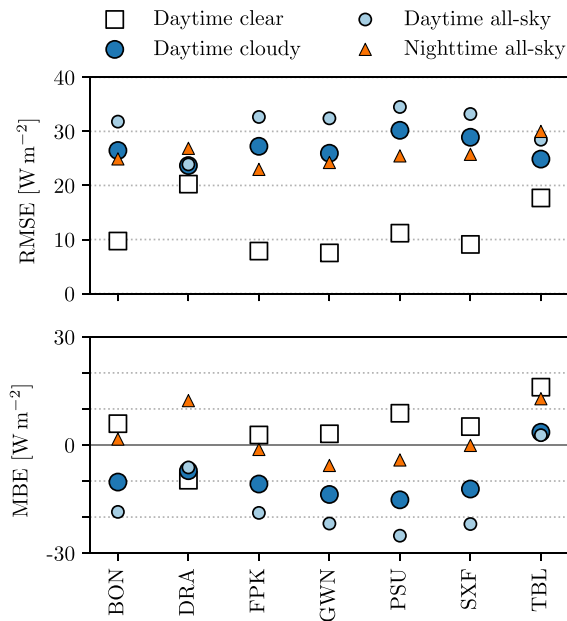
FIG. 9. The RMSE and MBE between the measured and modeled $F_0^\downarrow$ (W m^{-2}) for the seven SURFRAD stations and four evaluated cases: (1) daytime clear-sky, (2) daytime cloudy-sky, (3) daytime all-sky (clear or cloudy), and (4) nighttime all-sky (clear or cloudy). For the daytime cloudy-sky, daytime all-sky, and nighttime all-sky cases, $F_0^\downarrow$ is modeled using the SCOPE estimated values of τ, z_T, and Δz. Negative MBE values (MBE < 0) correspond to the model under-predicting $F_0^\downarrow$, which can be attributed to SCOPE under-predicting τ, over-predicting z_T, or over-predicting Δz.

from the method attempting to estimate clouds during clear-sky periods, a threshold-based heuristic is used to classify each timestamp as clear or cloudy. Based on empirical testing, a threshold of 0.05 on the mean error between the clear-sky modeled F_i^* ($\tau = 0$) and measured F_i^* for channels 11 and 13–15 is sufficiently accurate for the purposes of this study. If a time instance is identified as clear, the method sets $\tau = 0$ and moves on to the next time step. Otherwise, the method estimates τ, z_T, and Δz using the two-step approach detailed in Algorithm 1. Figure 8 shows that SCOPE can achieve similar F_i^* errors for all seven stations and ten channels for the daytime cloudy and all-sky cases. Figure 9 shows similar $F_0^\downarrow$ errors between the daytime cloudy and all-sky cases, but with an ~5 W m^{-2} larger negative bias for the daytime all-sky case for five of the seven sites. These results indicate that although SCOPE is more accurate when restricted to known cloudy periods, SCOPE can still be used in cases where the clear/cloudy classification is not known *a priori*, e.g., for sites without GHI data or during nighttime periods.

D. Nighttime all-sky periods

As a final test, SCOPE is evaluated on all-sky conditions at night ($\theta_z > 85°$). The setup is the same as the daytime all-sky case (see Sec. IV C), with one modification: we include a temperature inversion at 1 km in the AFGL midlatitude summer profile used by the radiative model. Based on empirical testing, the temperature inversion is

necessary to achieve error metrics similar to the daytime cases. Note that while there are data sources for temperature profiles at night, e.g., atmospheric sounding, such data are not considered in order to minimize data dependencies and therefore maximize the number of sites where the proposed method can be applied. Figures 8 and 9 show the F_i^* and $F_0^\downarrow$ errors, respectively, for the nighttime all-sky periods. The nighttime all-sky F_i^* error metrics are similar to the daytime all-sky case, except for channel 7 where the lack of the reflected solar component at night lowers the F_i^* RMSE to ~0.4 and MBE to ~0.3. For $F_0^\downarrow$, the nighttime all-sky RMSE and MBE are smaller than the daytime all-sky results for all stations except DRA and TBL. However, the nighttime all-sky $F_0^\downarrow$ RMSE for DRA and TBL only increases by ~3 W m^{-2} compared to the daytime all-sky case. In summary, the results indicate that SCOPE can be used during both day and night with similar accuracy.

V. CONCLUSIONS

The SCOPE method for real-time, direct estimation of cloud optical properties from high-resolution longwave remote sensing data is presented. By considering only the longwave spectrum, the method provides a unified approach to estimating cloud properties during day or night. The SCOPE method builds upon a two-stream, spectrally resolved radiative model, leverages publicly available satellite imagery from GOES-R, and requires minimal ground telemetry as inputs (only ambient temperature and relative humidity), which can be provided by a standard weather station or numerical weather prediction models. In addition, although SCOPE is evaluated on a GOES-R satellite (GOES-16), the method is compatible with other high-refresh satellites, e.g., the geostationary Himawari satellites that face the Eastern Hemisphere. Furthermore, SCOPE has minimal data dependencies, with a linear correction to standard atmospheric profiles, which allows SCOPE to be applied to a wide range of surface conditions and locations. Finally, the Python-based implementation of the method has a total wall-clock run time of ~1 s per time instance t, which is sufficiently fast for latency constrained applications, such as solar irradiance and power forecasting.

The performance of SCOPE is evaluated using a full year of data (1/1/2018–12/31/2018) from seven locations across the United States and for four cases: daytime clear-sky, daytime cloudy-sky, daytime all-sky (clear and cloudy), and nighttime all-sky. For each location and case, SCOPE estimates cloud optical properties from the upwelling longwave radiative flux at the top of the atmosphere, with the results evaluated against satellite measurements. Then, the estimated properties are used to model the downwelling longwave radiative flux at the surface and compared against ground measurements. SCOPE achieves downwelling longwave RMSE within instrument uncertainty (10 W m^{-2}) for four of the seven locations during daytime clear-sky conditions. Additionally, SCOPE achieves similar performance for daytime cloudy-sky, daytime all-sky, and nighttime all-sky conditions for all sites, with the downwelling longwave RMSE in the range of 23.0–34.5 W m^{-2}. The results indicate that SCOPE can accurately estimate cloud optical properties during both day and night. Coupled with its low latency, SCOPE is, therefore, suitable for
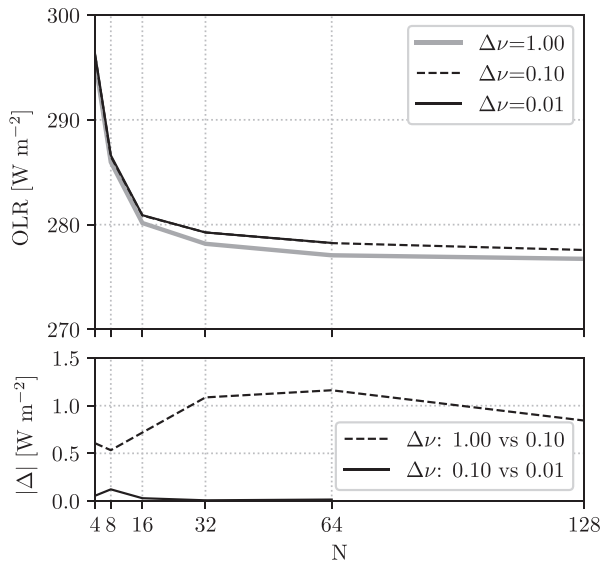
FIG. 10. Comparison of the clear-sky OLR as a function of the number of atmospheric layers (N) and spectral resolution ($\Delta\nu$) of the radiative model. All other model parameters are constant: $T_a = 294$ K, $\phi = 50\%$, and $\tau = 0$. Top: the broadband OLR (integrated over $\nu \in (0, 3000]$ cm^{-1}) vs N for $\Delta\nu \in \{0.01, 0.10, 1.00\}$ cm^{-1}. For each $\Delta\nu$, the model converges toward ~278 W m^{-2}. Bottom: the absolute difference ($|\Delta|$) between the OLR of the three $\Delta\nu$ values. The $\Delta\nu = 0.01$ cm^{-1} data end at $n = 64$ as the $n = 128$ case crashed due to insufficient memory.

providing accurate real-time estimates of cloud optical properties for solar forecasting applications.

ACKNOWLEDGMENTS

APPENDIX A: ERROR METRICS

Here, the error metrics used in this study are explicitly defined: mean bias error (MBE) and root mean square error (RMSE),

$$\text{MBE} = \frac{1}{n}\sum_{i=1}^{n}(\widehat{y}_i - y_i), \qquad (A1)$$

$$\text{RMSE} = \sqrt{\frac{1}{n}\sum_{i=1}^{n}(\widehat{y}_i - y_i)^2}, \qquad (A2)$$

where n is the number of samples, y is the target variable, and $\widehat{y}$ is the predicted value of the target variable. Based on these definitions,

TABLE III. Convergence of the clear-sky broadband OLR (W m^{-2}) as the number of layers (N) increases, for $\Delta\nu \in \{1.00, 0.10, 0.01\}$ cm^{-1}. For each N_i, the change in OLR ($|\Delta|$) is reported relative to the OLR from the previous N_{i-1}.

n	$\Delta\nu = 1.00$ cm^{-1} OLR (W m^{-2})	$|\Delta|$ (%)	$\Delta\nu = 0.10$ cm^{-1} OLR (W m^{-2})	$|\Delta|$ (%)	$\Delta\nu = 0.01$ cm^{-1} OLR (W m^{-2})	$|\Delta|$ (%)
4	295.611	…	296.217	…	296.272	…
8	285.962	3.26	286.495	3.28	286.617	3.26
16	280.156	2.03	280.874	1.96	280.903	1.99
32	278.173	0.71	279.260	0.57	279.253	0.59
64	277.077	0.39	278.239	0.37	278.254	0.36
128	276.739	0.12	277.583	0.24	[a]	[a]

[a]Cases that failed to run due to memory issues.

MBE > 0 corresponds to over-prediction and MBE < 0 to under-prediction.

APPENDIX B: GRID INDEPENDENCE

The radiative model is tuned to meet the requirement of real-time application of SCOPE. This requires balancing model precision and accuracy with computational time, which are primary functions of the number of atmospheric layers and spectral resolution. Given the 5-min update schedule for the GOES-R CONUS scans, we seek a model configuration with guaranteed run times under 1-min using readily available computing resources, e.g., a standard workstation-class machine with a 4-core CPU and 8 GB of RAM.

The number of atmospheric layers [n ($-$)] and the spectral resolution ($\Delta\nu$ cm^{-1}) are selected by a grid convergence test. The clear-sky broadband OLR is computed as a function of n and $\Delta\nu$, with all other parameters being constant. The AFGL midlatitude summer profile is selected to allow comparisons against previous work.[11] Figure 10 and Table III present the results of the grid convergence test under clear-sky conditions. Table III summarizes the convergence of the clear-sky broadband OLR as the number of atmospheric layers and spectral resolution increase, with all other parameters fixed. Note that no results are available for the 128-layer, 0.01 cm^{-1} case due to an out-of-memory issue on the machine used for testing.

The results show that the model performance is more dependent on N than $\Delta\nu$, with the OLR changing by less than 0.1 W m^{-2} by going from $\Delta\nu = 0.10$ cm^{-1} to 0.01 cm^{-1}. In addition, going from 32 to 64 layers for $\Delta\nu = 0.10$ cm^{-1} changes the broadband OLR by $<1\%$. Therefore, a configuration of 32-layers and $\Delta\nu = 0.10$ cm^{-1} is selected to balance between the model performance and computing times ($\ll$ 1-min per run).

APPENDIX C: ADDITIONAL FIGURES

Figures 11–16 show F_i^* as a function of P_w during daytime clear-sky periods for the BON, DRA, FPK, GWN, SXF, and TBL stations. The proposed SCOPE method is seen to be robust over climate-diverse locations.
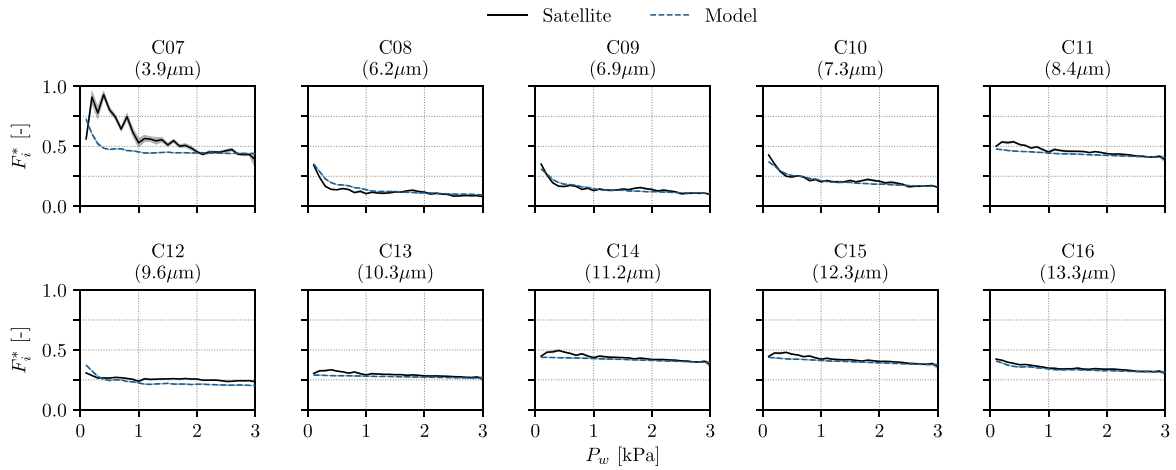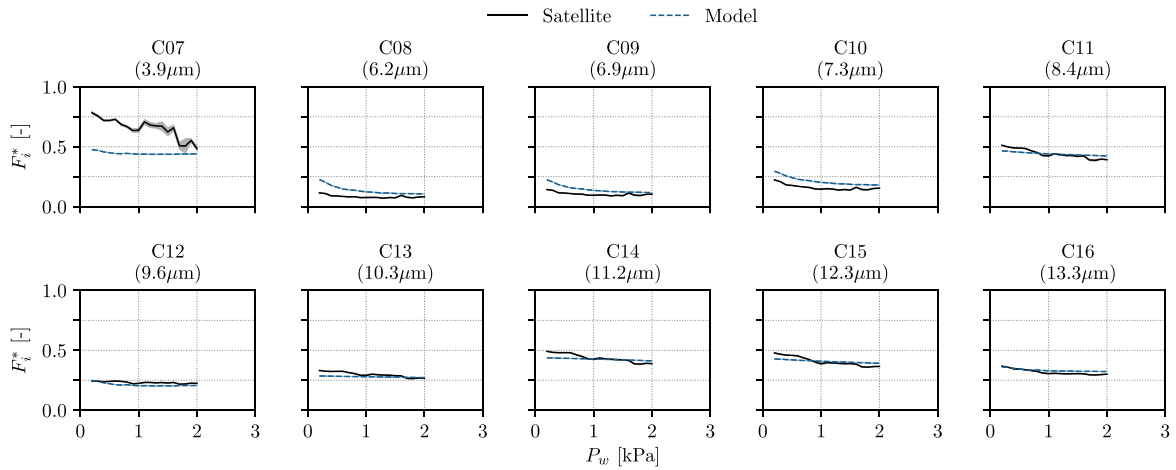
FIG. 11. The same as Fig. 7, but for the BON station.

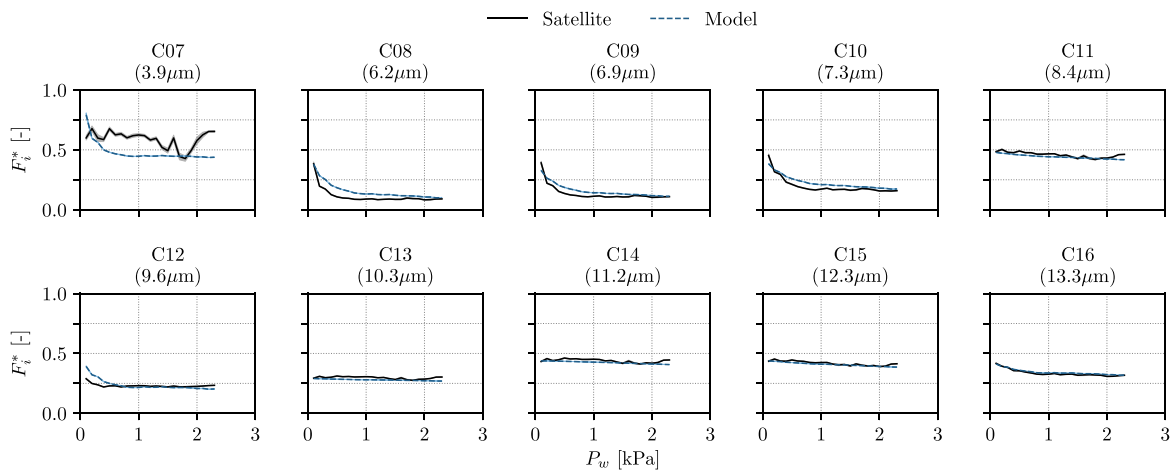**FIG. 12.** The same as Fig. 7, but for the DRA station.

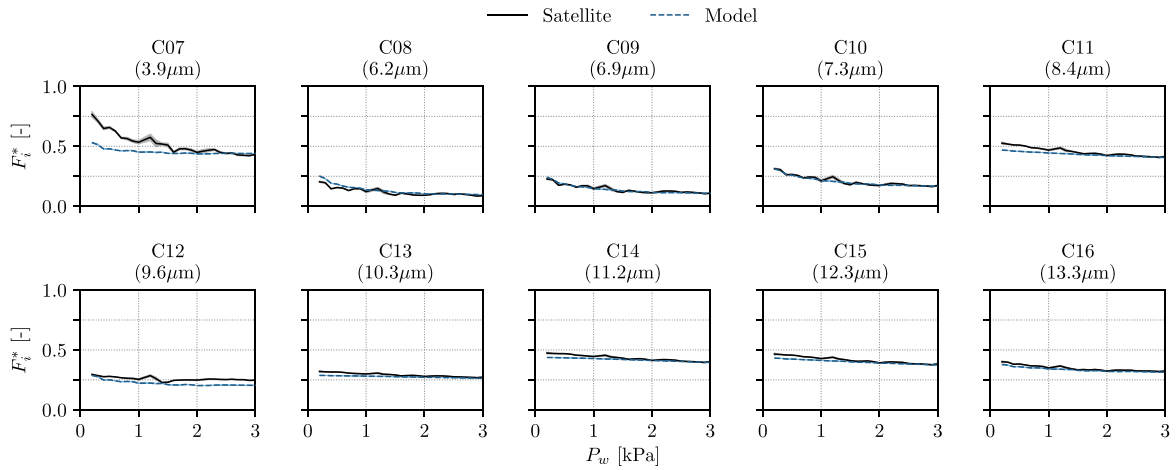**FIG. 13.** The same as Fig. 7, but for the FPK station.

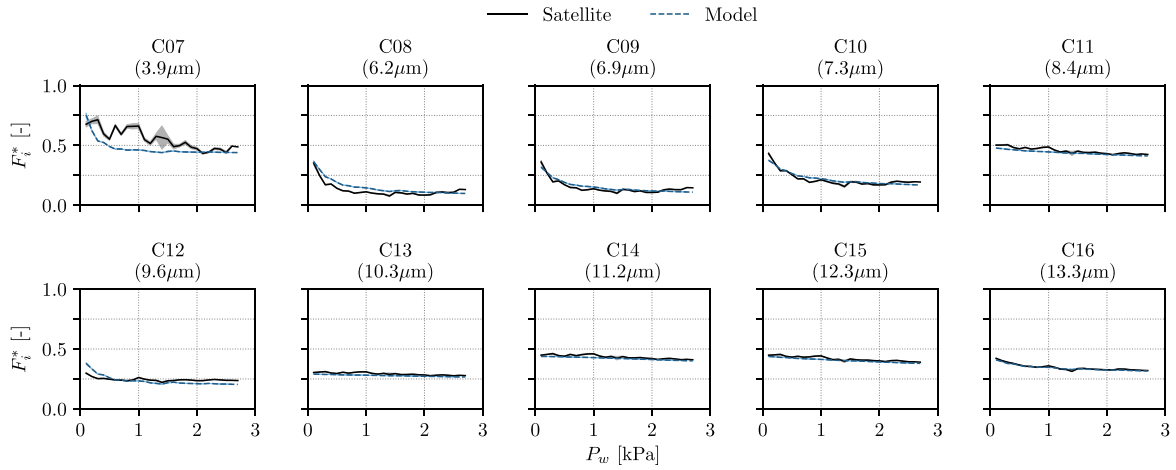**FIG. 14.** The same as Fig. 7, but for the GWN station.

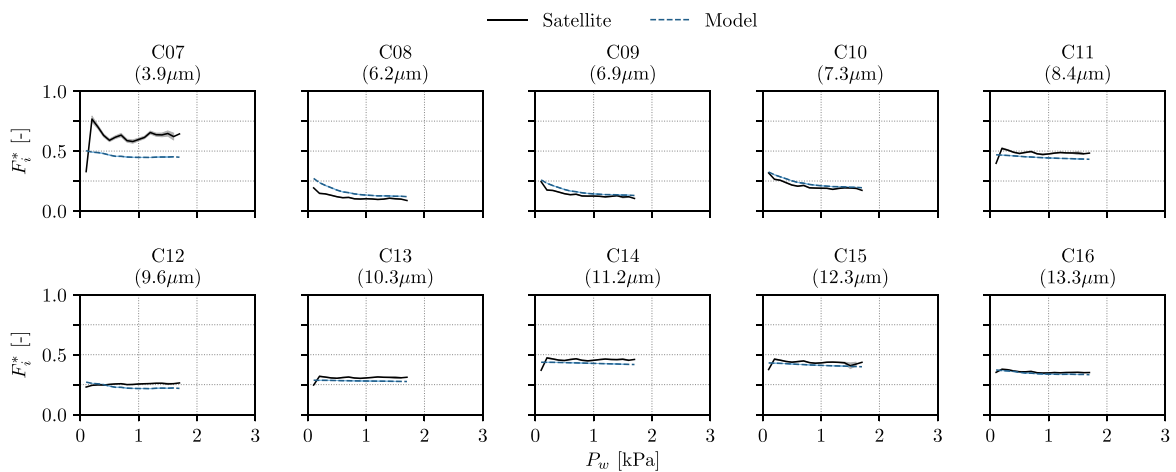**FIG. 15.** The same as Fig. 7, but for the SXF station.

FIG. 16. The same as Fig. 7, but for the TBL station.

REFERENCES

[1] R. Marquez, V. Gueorguiev, and C. F. M. Coimbra, "Forecasting of global horizontal irradiance using sky cover indices," J. Sol. Energy Eng. **135**, 0110171 (2012).

[2] R. Marquez and C. F. M. Coimbra, "Intra-hour DNI forecasting methodology based on cloud tracking image analysis," Sol. Energy **91**, 327–336 (2013).

[3] Y. Chu, H. T. C. Pedro, L. Nonnenmacher, R. H. Inman, Z. Liao, and C. F. M. Coimbra, "A smart image-based cloud detection system for intra-hour solar irradiance forecasts," J. Atmos. Oceanic Technol. **31**, 1995–2007 (2014).

[4] Y. Chu, M. Li, H. T. C. Pedro, and C. F. M. Coimbra, "Real-time forecasting of solar irradiance ramps with smart image processing," Sol. Energy **114**, 91–104 (2015).

[5] D. P. Larson, L. Nonnenmacher, and C. F. M. Coimbra, "Day-ahead forecasting of solar power output from photovoltaic plants in the American Southwest," Renewable Energy **91**, 11–20 (2016).

[6] D. P. Larson and C. F. M. Coimbra, "Direct power output forecasts from remote sensing image processing," J. Sol. Energy Eng. **104**, 021011 (2018).

[7] M. Li, Y. Chu, H. T. C. Pedro, and C. F. M. Coimbra, "Quantitative evaluation of the impact of cloud transmittance and cloud velocity on the accuracy of short-term DNI forecasts," Renewable Energy **86**, 1362–1371 (2016).

[8] C. W. Chow, B. Urquhart, M. Lave, A. Dominguez, J. Kleissl, J. Shields, and B. Washom, "Intra-hour forecasting with a total sky imager at the UC San Diego solar energy testbed," Sol. Energy **85**, 2881–2893 (2011).

[9] J. Li, W. P. Menzel, and A. J. Schreiner, "Variational retrieval of cloud parameters from goes sounder longwave cloudy radiance measurements," J. Appl. Meteorol. **40**, 312–330 (2001).

[10] A. Walther and A. K. Heidinger, "Implementation of the daytime cloud optical and microphysical properties algorithm (DCOMP) in PATMOS-X," J. Appl. Meteorol. Climatol. **51**, 1371–1390 (2012).

[11] M. Li, Z. Liao, and C. F. M. Coimbra, "Spectral model for clear sky atmospheric longwave radiation," J. Quant. Spectrosc. Radiative Transfer **209**, 196–211 (2018).

[12] T. J. Schmit, M. M. Gunshor, W. P. Menzel, J. J. Gurka, J. Li, and A. S. Bachmeier, "Introducing the next-generation advanced baseline imager on GOES-R," Bull. Am. Meteorol. Soc. **86**, 1079–1096 (2005).

[13] M. Li, Y. Jiang, and C. F. M. Coimbra, "On the determination of atmospheric longwave irradiance under all-sky conditions," Sol. Energy **144**, 40–48 (2017).

[14] B.-Y. Kim, K.-T. Lee, J.-B. Jee, and I.-S. Zo, "Retrieval of outgoing longwave radiation at top-of-atmosphere using Himawari-8 AHI data," Remote Sens. Environ. **204**, 498–508 (2018).

[15] M. Li and C. F. M. Coimbra, "On the effective spectral emissivity of clear skies and the radiative cooling potential of selectively designed materials," Int. J. Heat Mass Transfer **135**, 1053–1062 (2019).

[16] R. V. Kochanov, I. E. Gordon, L. S. Rothman, P. Wcisło, C. Hill, and J. S. Wilzewski, "HITRAN application programming interface (HAPI): A comprehensive approach to working with spectroscopic data," J. Quant. Spectrosc. Radiative Transfer **177**, 15–30 (2016).

[17] E. J. Mlawer, V. H. Payne, J.-L. Moncet, J. S. Delamere, M. J. Alvarado, and D. C. Tobin, "Development and recent evaluation of the MT_CKD model of continuum absorption," Philos. Trans. R. Soc. London A **370**, 2520–2556 (2012).

[18] M. Li, H. B. Peterson, and C. F. M. Coimbra, "Radiative cooling resource maps for the contiguous united states," J. Renewable Sustainable Energy **11**, 036501 (2019).

[19] H. Lee and R. Buckius, "Scaling anisotropic scattering in radiation heat transfer for a planar medium," J. Heat Transfer **104**, 68–75 (1982).

[20] Z. Liao, M. Li, and C. F. Coimbra, "Anisotropic corrections for the downwelling radiative heat transfer flux from various types of aerosols," Int. J. Heat Mass Transfer **136**, 1006–1016 (2019).

[21] D. K. Edwards, "The plating algorithm for radiation script-F transfer factor," J. Heat Transfer **108**, 237–238 (1986).

[22] M. Li, Z. Liao, and C. F. M. Coimbra, "Efficient model for evaluation of spectral and vertical distributions of atmospheric longwave radiation," in International Heat Transfer Conference (2018), Vol. 16.

[23] R. H. Inman, J. G. Edson, and C. F. M. Coimbra, "Impact of local turbidity estimation on clear sky models for direct normal irradiance," Sol. Energy **117**, 125–138 (2015).